



Innovative microkinetic modelling-supported structure–activity analysis of Ni/ZSM-5 during vapor-phase hydrogenation of levulinic acid

Hue-Tong Vu^{a,b,1}, Žan Lavrič^{b,c,1}, Andrii Kostyniuk^b, Goran Dražič^b, Miha Grilc^{b,c}, Blaž Likozar^{b,d,e,f}, Nataša Zabukovec Logar^{b,c}, Petar Djinović^{b,c,*}, Nataša Novak Tušar^{b,c,*}

^a Mientrung Industry and Trade College, Tuy Hoa, Phu Yen, Viet Nam

^b National Institute of Chemistry, Hajdrihova 19, 1000 Ljubljana, Slovenia

^c University of Nova Gorica, Vipavska 13, 5000 Nova Gorica, Slovenia

^d Faculty of Polymer Technology, Ozare 19, 2380 Slovenj Gradec, Slovenia

^e Pulp and Paper Institute, Bogišičeva ulica 8, 1000 Ljubljana, Slovenia

^f University of Ljubljana, Kongresni Trg 12, 1000 Ljubljana, Slovenia

ARTICLE INFO

Keywords:

Property–activity relationship
Ni/ZSM-5
Levulinic acid vapor-phase hydrogenation
Microkinetic modeling
Product distribution

ABSTRACT

The study examines Ni/ZSM-5 catalysts in vapor phase hydrogenation of levulinic acid (LA) under continuous flow conditions (ambient pressure, 210–250 °C). Advanced characterization revealed the interplay between Al and Ni. This was further reinforced by new approach of microkinetic modeling, which demonstrates a pioneering work on mathematical description of pulse H₂ sorption, TPD kinetics, DRIFT-supported determination of sorption energy barriers and (de)sorption kinetics. The Ni/ZSM-5 (3.7 wt.% Ni, Si/Al = 28) emerged as the optimal choice for obtaining γ -valerolactone (GVL) as the desired product. Al-rich catalysts with high acid site amounts and low metallic Ni active site concentrations favored esterification, reducing hydrogenation activity, and impeding further hydrogenation of GVL to pentanoic/valeric acid (PA). To enhance PA formation, Ni/ZSM-5 (4 wt.% Ni, Si/Al = 750) with a high Si/Al ratio, was identified as crucial. The combination of described experiments and modelling is demonstrated beneficial for insightful investigation of the structure–activity relationship of Ni/ZSM-5 or any other mono/bi-functional catalysts.

1. Introduction

The current environmental crisis is contributed mainly by the massive CO₂ emissions associated with heavy reliance on fossil resources. Biomass conversion was identified as one of the solutions to shift away from non-renewable energy resources owing to the ubiquity of lignocellulosic biomass, which can be utilized as a supplementary feedstock [1,2]. Moreover, non-edible lignocellulose, e.g., agricultural and forestry residues are renewable, and abundant, making it a highly attractive carbon source for chemical industries [3–5]. Over the last few decades, there have been numerous studies on the transformation of lignocellulose into commodity chemicals, i.e., levulinic acid, formic acid and furfural [6–8]. Among these, the acid-catalyzed hydrolysis producing levulinic acid (LA) as the main product has been established commercially to meet the rising demand for this versatile compound with an estimated compound annual growth rate of 12.55 % in

2022–2027 period [9,10]. LA can be found in various industrial sectors as reported in [11]. Furthermore, LA can also be converted into γ -valerolactone (GVL), pentanoic/valeric acid (PA) as well as pentanoate/valerate esters. These compounds are known precursors to the valeric biofuels family [12,13], which is a sustainable supplement for the current fossil-based fuel supplies. Thus, the transformation of LA into GVL and PA has been extensively studied [14–16]. Several studies emphasized on employing continuous flow setup [17–21], which is considered one of the technologies that can make significant difference towards sustainable production [22].

The conversion of LA can be carried out using different catalytic processes [23–27]. However, heterogeneous catalysis is exclusively discussed in this study. It is widely accepted that the hydrogenation of LA undergoes a multi-step reaction including hydrogenation and dehydration, illustrated in Scheme 1 [28]. Consequently, the catalysts for this reaction require both metallic and acidic functionalities [14]. In

* Corresponding authors at: National Institute of Chemistry, Hajdrihova 19, 1000 Ljubljana, Slovenia.

E-mail addresses: petar.djinovic@ki.si (P. Djinović), natasa.novak.tusar@ki.si (N. Novak Tušar).

¹ These authors contributed equally to this work.

addition to the state-of-art catalyst, Ru supported on activated carbon [29], there are numerous catalytic systems which have been investigated: precious metals (Pt, Ru) [17,23,30,31], transition metals (Ni, Cu) [16,32-34] or multi-component catalysts [21,34-36]. Among these, Ni supported on ZSM-5 zeolites show great potential for LA hydrogenation [37]. Despite numerous advantages of the bifunctional Ni/ZSM-5, an effective, robust and cheap catalyst with great abundance in acidic sites, there are only few studies carried out using Ni/ZSM-5 catalytic systems for the hydrogenation of LA, and a limited number that used fixed-bed reactor [38-41]. Moreover, Ni/ZSM-5 exhibited excellent stability without considerable changes even after 3 reaction cycles at 320 °C for 4 h [39]. The reaction pathway via angelica lactone (AL) seems dominant in vapor phase with respect to that via 4-hydroxypentanoic acid (HPA) regardless of the reaction conditions ($T \geq 240$ °C, atmospheric pressure) and choice of solvents, i.e., water, ethanol or solvent-free. The hydrogenation activity was found strongly dependent on the number of available Ni sites, which might decrease due to sintering or aggregation [38,39]. Regarding the influence of acidic properties of ZSM-5 supports, it is not trivial to identify the roles of each type, i.e., Brønsted and Lewis acid sites (BAS and LAS, respectively) in the conversion of LA to GVL, which are both relevant for high GVL selectivity. On the other hand, the strong BAS of ZSM-5, with respect to SiO_2 and Al_2O_3 [38], are beneficial for the ring-opening of GVL forming PA. It is evidenced that the hydrogenation of LA is sensitive to both metallic and acidic catalytic functionality, which can be regulated to steer selectivity. For example, the modification of Ni supported ZSM-5 catalyst with W leads to a considerably boosted PA selectivity, from 28 % to 65 %, as well as a higher LA conversion (40 % vs. 28 %) in comparison with unmodified counterpart under identical conditions (10 % LA aqueous solution, 270 °C and ambient pressure). The higher catalytic performance is attributed to the tungsten induced strengthening of BAS [41]. Furthermore, the acidic properties of ZSM-5 zeolites can also be tailored in a post treatment method by ion exchange with alkaline cations, e.g., potassium (K) [40], or following a bottom-up approach via varying the molar ratio of Si to Al precursors during synthesis. The vapor-phase hydrogenation of LA has several advantages over the liquid-phase, as it omits the issues caused by the poor solubility of hydrogen in solvents and additional mass transfer resistance, both resulting in lower availability of hydrogen on the catalyst surface.

The focus of this study was to investigate the property-activity relationship of Ni/ZSM-5 catalysts in the vapor-phase hydrogenation of LA. The obtained findings could be used to tailor product distribution towards desired product. We introduce a new approach combining experimental and kinetic investigation for the vapor-phase hydrogenation of LA with *iso*-propanol (IPA) in a fixed-bed reactor under moderate temperatures (210–250 °C) and ambient pressure. The ZSM-5 supports with various molar ratio of Si to Al ($n_{\text{Si}}/n_{\text{Al}}$) were prepared using a “green” organic-template free method in attempt to maximize the sustainability of the whole process. This study is a continuation of our

previous work examining the close correlation between nickel and framework Al in ZSM-5 in a quantitative manner using X-ray absorption spectroscopy supplemented with XRD, TEM and NMR [37]. Additionally, the study served as a demonstration of new methodology for determining relevant parameters of adsorption and desorption kinetics, obtained by quantitative modelling and regression analysis of experimental results from pulse chemisorption, temperature programmed desorption and diffuse reflectance infrared Fourier transform spectroscopy. These parameters were further incorporated in the microkinetic model, where surface kinetics was also determined by simultaneous regression analysis of all catalytic performance results measured for each catalyst type.

2. Experimental

2.1. Synthesis of bifunctional Ni/ZSM-5 catalysts

The H^+ -form zeolites (ZSM-5) with different Si to Al ratios (13, 21 and 28) were synthesized using a green template-free method followed by NH_4^+ ion exchange and subsequent thermal treatment as reported in [37,42]. Nickel was deposited by incipient wetness impregnation. A predetermined quantity of Ni precursor ($\text{Ni}(\text{NO}_3)_2 \cdot 6\text{H}_2\text{O}$, Sigma Aldrich, 99.999 %) was dissolved in 1 mL of deionized water. The aqueous solutions of Ni salts were added dropwise to preheated H-ZSM-5 (at 60 °C for 15 min) and ground well. The obtained solids were dried overnight at room temperature (RT) and were further calcined in air at 500 °C for 2 h. The obtained catalysts are referred to as xNi/ZSM-5-y with x and y representing Ni content (wt.%) and Si to Al molar ratios, respectively.

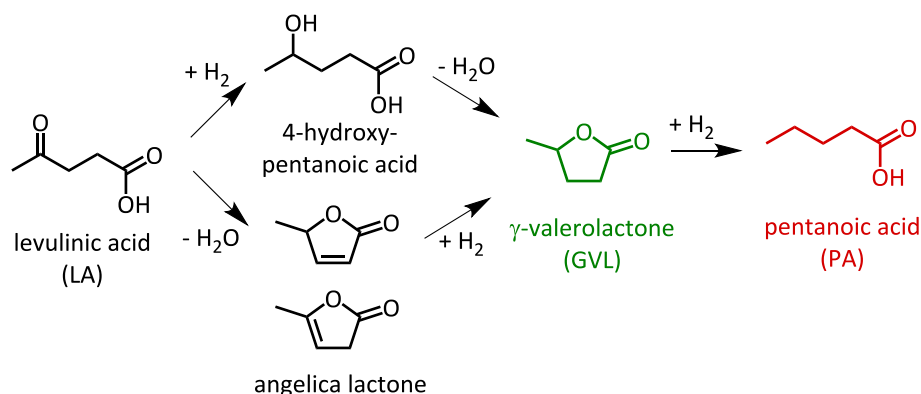
Additionally, ZSM-5-750, purchased from Tosoh Company, was employed as a Si rich ZSM-5 to extend the spectrum of Si to Al ratios investigated. The synthesis procedure of Ni/ZSM-5-750 is similar to the one mentioned by Kostyniuk et al. [43].

2.2. Catalyst characterization

The structural properties were characterized by a PANalytical X'Pert PRO MPD X-ray diffractometer ($\text{CuK}\alpha_1 = 0.154$ nm). The powder X-ray diffraction patterns were recorded at room temperature in the 2θ range from 5 to 70° with 0.034° increments.

N_2 sorption isotherms were recorded on a Quantachrome Autosorb iQ3 gas sorption analyzer at 77 K. Prior to the measurements, the samples were evacuated at 250 °C under vacuum for 10 h. The specific surface area (A_{BET}) and specific total pore volume (V_{p}) were determined using the Brunauer-Emmett-Teller (BET) model and single point ($p/p_0 = 0.97$) method, respectively.

Diffuse reflectance infrared Fourier transform spectroscopy (DRIFTS) was conducted on a Perkin Elmer Frontier spectrometer equipped with a MCT detector and a DiffusIR cell from Pike Scientific. Prior to the saturation with pyridine, the samples were degassed at



Scheme 1. Reaction pathways for conversion of LA into γ -valerolactone and pentanoic acid.

250 °C under N₂ flow (50 mL min⁻¹) for 1 h. The sample was cooled to 80 °C, at which the pyridine saturation was carried out by flushing the samples with a N₂ flow (50 mL min⁻¹) through a saturator filled with liquid pyridine for 30 min. The physisorbed pyridine was then removed under a N₂ flow of 50 mL min⁻¹ at 80 °C for 2 h. The spectra were recorded in the wavenumber range from 500 to 4000 cm⁻¹ with a spectral resolution of 2 cm⁻¹. The IR bands centered at 1554 cm⁻¹ and 1445 cm⁻¹ are ascribed to Brønsted (BAS) and Lewis acid sites (LAS), respectively. The ratio of BAS-to-LAS ($n_{\text{BAS}}/n_{\text{LAS}}$) was calculated using the intensity ratio of these two bands.

Temperature-programmed reduction with H₂ (H₂-TPR) was performed with a Micromeritics AutoChem II Chemisorption Analyser (Micromeritics, USA). 100 mg of the sample was inserted into a U-shaped quartz tube and degassed at 300 °C under argon (50 mL min⁻¹) for 30 min. Subsequently, to carry out the reduction of the samples, the gas flow was switched to 5 vol% H₂/Ar mixture (40 mL min⁻¹) and heated at a constant heating rate of 10 K min⁻¹ from RT to 900 °C. Hydrogen consumption was determined using a TCD detector and calibrated using Ag₂O. Based on Ni content and the H₂ consumption of each sample, the corresponding relative amount of Ni²⁺ reduced under identical conditions of H₂-TPR measurements was determined, assuming that the H₂-to-Ni stoichiometry is 1.

Temperature programmed desorption of NH₃ (NH₃-TPD) and pulse H₂ chemisorption-TPD were carried out using a AutoChem II Chemisorption Analyser (Micromeritics, USA). The desorbed gases were analyzed by a GSD 301 T3 Thermostar Mass Spectrometer. Similarly, the samples were degassed under the same conditions as prior to the H₂-TPR experiments. In a typical NH₃-TPD measurement, the samples were exposed to 40 mL min⁻¹ of ammonia (10 vol% NH₃ in He, 60 °C, 1 h) which was then switched to He (40 mL min⁻¹) to carry out the desorption experiments by heating the sample from 60 °C to 600 °C with a heating rate of 10 K min⁻¹. The amount of desorbed NH₃ was quantified using the MS fragment $m/z = 15$ and calibrated using 6 successive pulses of 1 mL of 10 vol% NH₃ in He. Based on the temperature at maximum NH₃ desorption (T_{des}), the acid sites were classified into strong ($T_{\text{des}} \geq 450$ °C), moderate (230 °C < $T_{\text{des}} < 450$ °C) and weak ($T_{\text{des}} \leq 230$ °C) [27].

The pulse H₂ chemisorption-TPD experiments were performed after sample reduction and degassing. The samples were cooled to 0 °C and saturated with 18 pulses ($V = 1$ mL) of 5 vol% H₂ in Ar (15 mL min⁻¹), which was then switched to Ar (15 mL min⁻¹) for desorption while increasing temperature to 500 °C. The MS fragment $m/z = 2$ was used to quantify the amount of desorbed H₂.

The Ni K-edge XANES (X-ray Absorption Near Edge Structure) and EXAFS (Extended X-ray Absorption Fine Structure) spectra of the Ni/ZSM-5 catalysts were measured at XAFS beamline of Elettra synchrotron Trieste in transmission detection mode at room temperature. The homogeneous pellets of samples were employed to obtain the optimal total absorption thickness of about 2 above the investigated absorption edge. The recorded EXAFS spectra were fitted using a combined FEFF model that contained all scattering paths used in the fit of the crystalline NiO, in which the relative coordination shell numbers N_{rel} of each shell were also allowed to vary, and scattering paths of O and Si neighbors found in case of Ni²⁺ cations attached to the zeolite framework via Ni-O-Si bridges [44]. Spectral deconvolution and fitting enabled the quantification of the two Ni-containing species for all the samples, namely bulk-like NiO oxides and Ni²⁺ attached to the ZSM-5 framework, also called as extra framework Ni²⁺ [34]. More details of the quantification of the relative amount of NiO nanoparticles (%NiO) can be found in [37].

The amount of NiO (n_{NiO} in mmol g⁻¹) was calculated based on total Ni content in the sample (w_{Ni} in wt.%), molar mass of Ni (M_{Ni}) and the relative amount of NiO (%NiO), in particular as $n_{\text{NiO}} = w_{\text{Ni}} \cdot \% \text{NiO} \cdot (M_{\text{Ni}})^{-1}$.

Scanning transmission electron microscopy (STEM) analysis was carried out on a Cs probe-corrected TEM/STEM Jeol ARM 200 CF

microscope coupled with a cold-FEG electron source at 80 kV. A Jeol Centurio 100 mm² Energy dispersive X-ray spectrometer (EDXS) was used for elemental analyses and mapping in scanning-transmission mode (STEM). The powdered samples were dispersed in ethanol, dried under ambient conditions and subsequently placed on a copper lacy-carbon coated TEM grid prior to analysis.

Scanning electron microscopy – energy dispersive X-ray (SEM-EDX) spectra were recorded on a Zeiss Supra 35 VP microscope (acceleration voltage 20 kV) equipped with a 100 mm² silicon drifted detector (SDD). The elemental content was determined using the INCA software.

2.3. Catalytic hydrogenation of levulinic acid in iso-Propanol (IPA)

The catalytic conversion of LA was carried out in a fixed-bed reactor Microactivity Reference reactor from PID Eng&Tech.

The catalysts were packed into the tubular reactor (inner diameter = 9 mm, length = 305 mm). Typically, 100 mg of catalyst was diluted with 100 mg of glass beads (both having particle size < 100 μm) and sandwiched by quartz wool plugs. The average length of catalyst bed was 5.5 mm. The reactor was heated and kept at 400 °C under a N₂ flow (30 mL min⁻¹) for 1 h. The gas stream was then switched to H₂ (30 mL min⁻¹) while holding at 400 °C. The catalyst reduction was performed for 2 h, after which the reactor was cooled down and kept at designated reaction temperature. The reaction mixture, i.e., 1 wt% of levulinic acid in iso-propanol solvent (IPA), was fed at a flow rate of 0.03 g min⁻¹ into the reactor using a Gilson HPLC pump. The liquid and H₂ streams merged and passed a 6-port valve into the tubular reactor. The tubular reactor and all the lines were hosted in a hot box and kept at 170 °C to prevent condensation. The gas mixture leaving the reactor was cooled to 0 °C in the liquid-gas condenser/separator. The gas products were analyzed by a micro GC Fusion (Inficon), which is connected at the output of the liquid-gas separator. No carbon containing gas product was detected. The liquid products were collected every hour after reaching the reaction steady state (typically 120 min) and analyzed by a GC-MS (Shimadzu, QP 2010) using a ZebronTM ZB-5MSi capillary column (60 m × 0.25 mm × 0.25 μm). The concentrations of the liquid reaction products were determined using calibration curves of commercial LA (97 %, Sigma-Aldrich), GVL (99 %, Sigma-Aldrich), AL (98 %, Sigma-Aldrich), PA (99 %-Sigma-Aldrich) and self-prepared PL and PP via external calibration technique. The relative errors of measured LA, GVL, AL and PL concentrations were below 5 %. The LA conversion, GVL, AL and PL yields were calculated as follow:

$$X_{\text{LA}} = \frac{n_{\text{LA,in}} - n_{\text{LA,out}}}{n_{\text{LA,in}}} \bullet 100\% \quad (1)$$

$$Y_{\text{GVL}} = \frac{n_{\text{GVL}}}{n_{\text{LA,in}}} \bullet 100\% \quad (2)$$

$$Y_{\text{AL}} = \frac{n_{\text{AL}}}{n_{\text{LA,in}}} \bullet 100\% \quad (3)$$

$$Y_{\text{PL}} = \frac{n_{\text{PL}}}{n_{\text{LA,in}}} \bullet 100\% \quad (4)$$

$$Y_{\text{PA}} = \frac{n_{\text{PA}}}{n_{\text{LA,in}}} \bullet 100\% \quad (5)$$

$$Y_{\text{PP}} = \frac{n_{\text{PP}}}{n_{\text{LA,in}}} \bullet 100\% \quad (6)$$

with $n_{\text{LA,in}}$ and $n_{\text{LA,out}}$ refer to the input and output molar amount of LA. n_{GVL} , n_{AL} and n_{PL} are the molar amounts of GVL, AL and PL, respectively, in the product mixtures.

2.4. Microkinetic model

The microkinetic model portrays the concentration of gas phase and

coverage of the catalyst's active sites as a function of time and catalyst bed length. The model was adjusted to both the temperature programmed and isothermal catalytic tests, where the main difference was the parameters, which were obtained during the regression analysis. The model for temperature programmed experiments considered axial convection in the void volume of the catalyst bed and adsorption and desorption kinetics, while the model for catalytic tests, besides the mentioned phenomena, also included surface reactions.

The rate of adsorption (r_j^{ads}) for adsorbate j at any time or axial coordinate increment, which depends on the adsorption rate constant (k_j^{ads}), the concentration of the adsorbing compound in the gas phase (C_j) and the fraction of the available vacant sites on the surface (θ_{VS}), were calculated with Equation Eq. 1.

$$r_j^{\text{ads}} = k_j^{\text{ads}} \cdot C_j \cdot \theta_{\text{VS}} \quad (1)$$

The rate of desorption (r_j^{des}) for the j -th compound depends on the desorption rate constant (k_j^{des}) and the corresponding surface coverage (Eq. (2)).

$$r_j^{\text{des}} = k_j^{\text{des}} \cdot \theta_j \quad (2)$$

The surface reaction rate (r_i^{surf}) for the reaction i depends on the reaction rate constant (k_i^{surf}) and the reactant(s) coverage (θ_j) for the i -th reaction (Eq. (3)).

$$r_i^{\text{surf}} = k_i^{\text{surf}} \cdot \prod_{\epsilon \in i} \theta_{j_1} \quad (3)$$

A reaction can also occur between reactants adsorbed on two different types of active sites. If such, the rate Eq. 3 becomes a rate Eq. (4).

$$r_i^{\text{surf}} = k_i^{\text{surf}} \cdot \theta_{j_1} \cdot \theta_{j_2} \quad (4)$$

Desorption and reaction rate constants were expressed as temperature dependent constants according to the Arrhenius law. Activation energy for the desorption ($E_{a_i}^{\text{des}}$) reaction was determined with non-isothermal TPD experiments for hydrogen and DRIFTS experiments for ethyl levulinate (EL) and IPA, while activation energy for reactions ($E_{a_i}^{\text{surf}}$) were determined from isothermal reaction experiments, conducted at different temperatures. Desorption constant (k_j^{des}) was calculated with Eq. (5), while reaction rate constant was calculated with Eq. (6).

$$k_i^{\text{des}}(T) = k_i^{\text{des}}(T_{\text{ref}}) \cdot \exp\left(\frac{E_{a_i}^{\text{des}}}{R} \cdot \left(\frac{1}{T_{\text{ref}}} - \frac{1}{T}\right)\right) \quad (5)$$

$$k_i^{\text{surf}}(T) = k_i^{\text{surf}}(T_{\text{ref}}) \cdot \exp\left(\frac{E_{a_i}^{\text{surf}}}{R} \cdot \left(\frac{1}{T_{\text{ref}}} - \frac{1}{T}\right)\right) \quad (6)$$

T_{ref} is the temperature, at which the activation energy for desorption and reaction were determined. If required, the pre-exponential factor (A_i^{surf}) is calculated with Eq. (7).

$$A_i^{\text{surf}} = k_i^{\text{surf}}(T_{\text{ref}}) \cdot \exp\left(\frac{E_{a_i}^{\text{surf}}}{R \cdot T_{\text{ref}}}\right) \quad (7)$$

Molar balances for gas concentrations (C_j) are the sum of convective (v_z represents linear velocity of fluid) and diffusive flux (D_j^e represents effective diffusion of the compound j) in the axial direction (z), as well as adsorption and desorption rates. Desorption rate is multiplied with the volume of the gas phase (V^G is the void volume in the bed) and divided by the total amount of the surface sites available in the bed (n_{TS}). The flux in radial direction was neglected, due to the high porosity of the bed, comprising small particles, which acted as static mixers and thus ensured uniform gas concentration in the radial dimension (Eq. (7)).

$$\frac{\partial C_j}{\partial t} = -\frac{\partial}{\partial z} [v_z \cdot C_j - D_j^e \cdot \frac{\partial C_j}{\partial z}] - r_j^{\text{ads}} + r_j^{\text{des}} \cdot \frac{n_{\text{TS}}}{V^G} \quad (8)$$

In case of non-isothermal TPD experiments, the catalyst bed length was much shorter than in catalytic experiments, and thus the diffusive flux term was omitted (Eq. (8)).

$$\frac{\partial C_j}{\partial t} = -\frac{\partial}{\partial z} [v_z \cdot C_j] - r_j^{\text{ads}} + r_j^{\text{des}} \cdot \frac{n_{\text{TS}}}{V^G} \quad (9)$$

The total amount of acid or metal active sites was calculated with surface sites density (q_{tot}) and the mass of the catalysts loaded in the reactor (Eq. (9)).

$$n_{\text{TS}} = q_{\text{tot}} \cdot m_{\text{cat}} \quad (10)$$

The void volume (V^G) depends on catalyst bed porosity (α) and the volume (V) of the reactor, where the catalyst is embedded (Eq. (10)).

$$V^G = \alpha \cdot V \quad (11)$$

Linear velocity (v_z) in the catalytic bed depends on the set volumetric flow rate (V) at ambient temperature (T_{AT}), tube cross-sectional area, temperature in the reactor (T) and bed porosity (Eq. (11)).

$$v_z(T) = \frac{4 \cdot \dot{V}}{\alpha \cdot \pi \cdot D^2} \cdot \left(\frac{T}{T_{\text{AT}}}\right) \quad (12)$$

The balance for surface coverages is presented in Eq. (12), where adsorption, desorption and surface reactions dictate the coverage fraction at each t and z for compound j .

$$\frac{\partial \theta_j}{\partial t} = r_j^{\text{ads}} \cdot \frac{V^G}{n_{\text{TS}}} + r_j^{\text{des}} \sum_i \pm r_i^{\text{surf}} \quad (13)$$

The balance for vacant sites considers all adsorption and desorption rates and surface reaction rates with non-stoichiometric reactions regarding reactants consumed and products formed (Eq. (13)).

$$\frac{\partial \theta_{\text{VS}}}{\partial t} = -\sum_j r_j^{\text{ads}} \cdot \frac{V^G}{n_{\text{TS}}} + \sum_j r_j^{\text{des}} \sum_i \pm r_i^{\text{surf}} \quad (14)$$

According to the molar balances of the components in the gas phase and on the catalyst surface, a system of partial differential equations (PDE) was designed at every increment of the fixed bed length (z from 0 to Z) and at any time increment (t from 0 to t_{end}). To solve the formulated system numerically, a MATLAB 2021b software was used. To speed up the regression and reduce the computational time, the PDE equations were modified into a system of ordinary differential equations (ODE). The concentration and surface coverage of each species at each z position were solved as a function of time with ODE 15 s solver, based on numerical differentiation formulas (NDF).

To be exact, 16 PDEs (8 for gas phase concentrations and 8 for surface coverages) were transferred into 1600 ODEs to calculate their value at 100 z locations $\{z \mid 0 \leq z \leq L\}$ all over the catalyst bed for each time increment until the steady state (LA – reaction test) or complete desorption (TPD-H₂ and ethyl levulinate (EL) or isopropanol (IPA) DRIFTS test) was accomplished. For all modelled experiments, the same algorithm was used, but with minor adjustments to the boundary conditions. The LA-reaction test was conducted with initial reactant concentration at the inlet of the fixed bed. The simulation was stopped, once the steady state was reached. Pulse H₂ chemisorption-TPD was performed with non-steady state boundary condition at the inlet with varying H₂ concentration. Also, the temperature was increased with a constant temperature ramp in the last part of the simulation, where desorption of H₂ took place. DRIFTS experiments were similar to pulse TPD experiment. The main difference between pulse TPD and DRIFTS simulation was the initial surface coverage fraction. Pulse TPD's surface coverage fraction was 0 at the beginning, while DRIFTS surface coverage fraction was 1, due to the different experimental procedures. The fractional coverage of the ethyllevulinate (EL) and isopropanol (IPA) was

estimated through temperature programmed desorption experiment carried out in the Spectrum1 FTIR spectrometer equipped with a reaction cell DiffusIR by Pike Scientific. The powdered samples were saturated overnight by EL or IPA vapors inside a laboratory drier at 60 °C. During the temperature programmed run, the sample was heated in argon flow from room temperature to 350 °C with a 10 °C ramp. The spectra were recorded using a LN₂ cooled MCT detector between 800 and 4000 cm⁻¹ with spectral resolution of 1 cm⁻¹ and 16 accumulations per scan. Intensity of the C-O and C-H stretching bands at 1724 and 2984 cm⁻¹ was followed to attain the temperature dependent coverage of EL and IPA, respectively.

During the regression analysis, activation energies and reaction rate constants at the reference temperature were determined. With the use of Nelder-Mead algorithm, the objective function was minimized, while the Levenberg-Marquardt algorithm was used for the determination of 95 % confidence intervals.

$$f(Ea_i^{\text{surf}}, Ea_i^{\text{des}}, k_j^{\text{ads}}, k_i^{\text{surf}}, k_j^{\text{des}}) = \sum_j^I (C_j^{\text{measured}} - C_j^{\text{calculated}}(Ea_i^{\text{surf}}, Ea_i^{\text{des}}, k_j^{\text{ads}}, k_i^{\text{surf}}, k_j^{\text{des}}))^2 \quad (15)$$

3. Results and discussion

3.1. Catalyst characterization

The synthesized catalysts and their elemental compositions are listed in Table 1, which can be categorized into two groups, i.e., variable Ni content (from 0.8 to 4.4 wt%) on the same support ZSM-5-21 ($n_{\text{Si}}/n_{\text{Al}} = 21$) and secondly, ca. 3.5 wt% Ni on ZSM-5 supports with various $n_{\text{Si}}/n_{\text{Al}}$ (from 13 to 750). Irrespective of Al and Ni content, all catalysts exhibit highly crystalline MFI-type structure as evidenced in XRD patterns (Fig. S1) displaying sharp reflections at 2θ of 7.9°, 8.9°, 23.0° and 23.8° characteristic for (011), (200), (051) and (033) planes of ZSM-5 zeolites. Additionally, a diffraction reflex at 2θ of 43.3° corresponding to (200) plane of NiO (PDF#01-089-5881), is observed for all of the Ni/ZSM-5 catalysts, except for the 0.8Ni/ZSM-5-21 catalyst due to the low Ni content and small crystal size that is below the detection limit of XRD [37]. Based on this reflection, the crystallite size of NiO was calculated using Scherrer equation. While 4.0Ni/ZSM-5-750 exhibits large NiO crystallites (ca. 46 nm), a smaller crystallite size is recorded for other Ni/ZSM-5 catalysts (ca. 20–23 nm). With respect to the textural properties, all the Ni/ZSM-5 catalysts exhibit similar isotherms, which can be categorized as type I, typical for the highly microporous ZSM-5 zeolites [45], with a small fraction of mesopores as deduced from the H4 hysteresis loop, Fig. S2. Consequently, the porous structure is analogous for all catalysts with a specific surface area of ca. 400 m²·g⁻¹ and a

specific pore volume of ca. 0.2 cm³·g⁻¹ irrespective of Al and Ni content. This is in good agreement with our previous study on Ni/ZSM-5 catalysts [37] confirming that the variation of Al content up to 2.5 wt.% and the introduction of Ni up to 4.4 wt.% have marginal influence in both the structural and textural of the obtained materials.

The acidic properties of the bifunctional Ni/ZSM-5 catalysts were examined by NH₃-TPD. In general, the recorded profiles of all catalysts feature two main groups of acid sites depending on the temperature at which the most intense desorption of NH₃ was detected (T_{des}). In particular, there are strong ($T_{\text{des}} \approx 400$ °C) and weak acid sites ($T_{\text{des}} \approx 200$ °C) (Fig. 1). Within the Ni/ZSM-5-21 series (Fig. 1, left), all NH₃-TPD profiles depict a 55 % of weak and 45 % of strong acid sites. The 0.8Ni/ZSM-5-21 displays slightly stronger acid sites as suggested by a shift to higher temperature of the strong acid sites peak. Nevertheless, the acid site density (ASD) of ca. 1.5 mmol·g⁻¹ was recorded for most of Ni/ZSM-5-21 catalysts (Table 1), except for 4.4Ni/ZSM-5-21 exhibiting

a slightly higher ASD (1.6 mmol·g⁻¹), probably due to the highest Ni content, which might provide additional Lewis acid sites [43]. Nevertheless, these findings suggest the acidic properties for Ni/ZSM-5-21 catalysts are similar, irrespective of Ni content and thus the influence of Ni on the acidity of ZSM-5-21 catalysts is marginal.

In contrast, the variation of Si to Al ratio of the Ni/ZSM-5 catalysts considerably altered its acidity (Table 1). In particular, a drop in ASD from 2.4 to 0.2 mmol·g⁻¹ was recorded for Ni/ZSM-5 catalysts when raising the Si/Al ratio up to 750. Owing to the lowest Si/Al ratio, 3.5Ni/ZSM-5-13 exhibits considerably higher ASD and consequently broader distribution of acid sites compared to the other two catalysts (3.4Ni/ZSM-5-21 and 3.7Ni/ZSM-5-28) as deduced by the shape of the NH₃-TPD profiles (Fig. 1, right). In addition to two main groups including the weak ($T_{\text{des}} \leq 230$ °C) and strong (230 °C < $T_{\text{des}} < 450$ °C) acid sites that were recorded for all the Ni/ZSM-5 catalysts, a group of acid sites with $T_{\text{des}} \geq 450$ °C was recorded for 3.5Ni/ZSM-5-13 (Table S1). As expected, the increase in Si/Al ratio leads to a loss in the number of strong acid sites from 0.31 to 0.02 mmol·g⁻¹. The ratios of weak acid sites to the strong acid sites were found to be 1.7, 1.2, and 1.1; a decreasing trend with increasing Si/Al ratio. This trend agrees well with the DRIFTS results of pyridine adsorption analysis (Fig. S3) and suggests an incomplete incorporation of Al into ZSM-5 framework resulting in the formation of extra framework Al (EFAL), which acts as weak acid sites/LAS. Indeed, more EFAL, also known as octahedral Al, was observed for Al rich ZSM-5 in a previous study [37].

The chemical environment of Ni was evaluated by X-ray absorption spectroscopy (XAS). Previously, by combining a handful of advanced techniques (XANES, EXAFS, TEM, Al-NMR and XRD), it was proven that

Table 1

Elemental content (wNi and wAl), Ni crystal size (nm) Si to Al molar ratio ($n_{\text{Si}}/n_{\text{Al}}$), specific surface area (A_{BET}), specific pore volume (V_p) and acid site density (ASD) of the Ni/ZSM-5 catalysts.

Catalysts	wNi ^a /wt.%	Ni crystal size ^b /nm	wAl ^a /wt.%	$n_{\text{Si}}/n_{\text{Al}}$ ^a	$A_{\text{BET}}/\text{m}^2\cdot\text{g}^{-1}$	$V_p/\text{cm}^3\cdot\text{g}^{-1}$	ASD ^c /mmol·g ⁻¹
0.8Ni/ZSM-5-21	0.8 ± 0.1	n.d.	1.8 ± 0.1	21	405	0.20	1.5
1.6Ni/ZSM-5-21	1.6 ± 0.1	n.d.	1.6 ± 0.1	21	443	0.20	1.5
3.4Ni/ZSM-5-21	3.4 ± 0.2	21	1.6 ± 0.1	21	425	0.20	1.5
4.4Ni/ZSM-5-21	4.4 ± 0.2	23	1.7 ± 0.1	21	375	0.19	1.6
3.5Ni/ZSM-5-13	3.5 ± 0.1	22	2.5 ± 0.1	13	441	0.22	2.4
3.7Ni/ZSM-5-28	3.7 ± 0.3	20	1.2 ± 0.2	28	410	0.20	1.2
4.0Ni/ZSM-5-750 ^d	4.0 ± 0.3	46	n.d.	750*	380	0.19	0.2

^aSEM-EDX; ^cXRD; ^eNH₃-TPD; n.d.: not determined; ^dcommercial support; *provided by Tosoh Co., Japan.

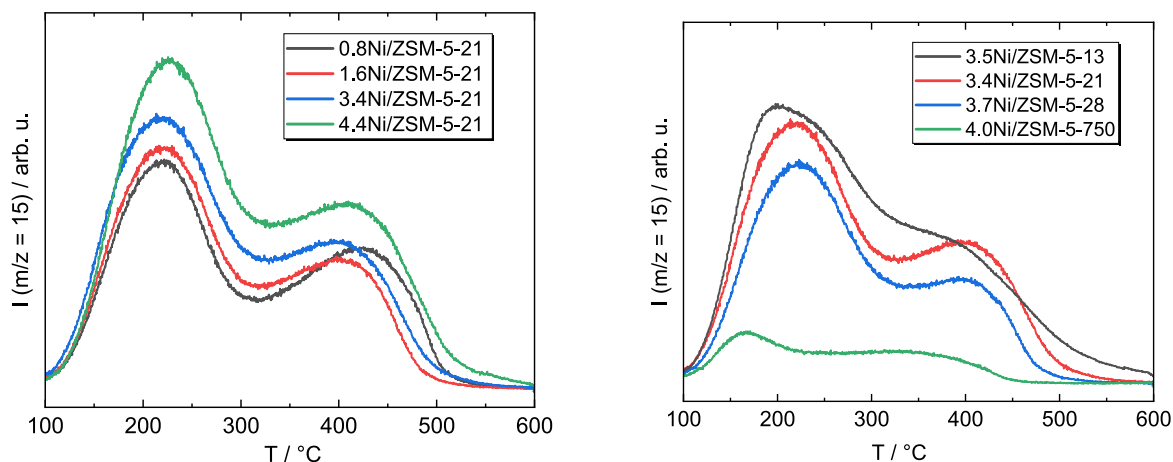


Fig. 1. NH_3 -TPD profiles of Ni catalysts ($w_{\text{Ni}} = 0.8\text{--}4.4$ wt.%) supported on ZSM-5-21 (left) and ca. 3.5 wt.% Ni on various ZSM-5 zeolites (right), i.e., 3.5Ni/ZSM-5-13 (black), 3.4Ni/ZSM-5-21 (red), 3.7Ni/ZSM-5-28 (blue) and 4.0Ni/ZSM-5-750 (green).

Table 2

Ni content, relative amount of crystalline NiO and extra framework Ni^{2+} cations (EFNi), number of NiO (n_{NiO}), H_2 consumption and relative amount of reduced Ni species below 700 °C of the bifunctional Ni/ZSM-5 catalysts.

Catalysts	$w_{\text{Ni}}^a/\text{wt.}\%$	$\% \text{NiO}^b$	$\% \text{EFNi}^b$	$n_{\text{NiO}}^c/\text{mmol}\cdot\text{g}^{-1}$	H_2 consumption ^d / $\text{mmol}\cdot\text{g}^{-1}$	$\% \text{Reduced Ni}^{2+}$ ($T \leq 700$ °C) ^d
3.7Ni/ZSM-5-28	3.7 ± 0.3	$71 \% \pm 5 \%$	$29 \% \pm 5 \%$	0.448	0.64	>99 %
3.5Ni/ZSM-5-13	3.5 ± 0.2	$41 \% \pm 5 \%$	$59 \% \pm 5 \%$	0.245	0.32	54 %
3.4Ni/ZSM-5-21	3.4 ± 0.2	$72 \% \pm 5 \%$	$28 \% \pm 5 \%$	0.417	0.36	61 %
4.4Ni/ZSM-5-21	4.4 ± 0.2	n.d.	n.d.	n.d.	0.37	49 %
1.6Ni/ZSM-5-21	1.6 ± 0.1	$75 \% \pm 5 \%$	$25 \% \pm 5 \%$	0.204	n.d.	n.d.
0.8Ni/ZSM-5-21	0.8 ± 0.1	$73 \% \pm 5 \%$	$27 \% \pm 5 \%$	0.100	n.d.	n.d.
4.0Ni/ZSM-5-750	4.0 ± 0.3	n.d.	n.d.	n.d.	0.70	>99 %

^aSEM-EDX; ^bEXAFS [37]; ^c $n_{\text{NiO}} = w_{\text{Ni}} \cdot \% \text{NiO} \cdot (M_{\text{Ni}})^{-1}$; ^d H_2 -TPR; n.d.: not determined.

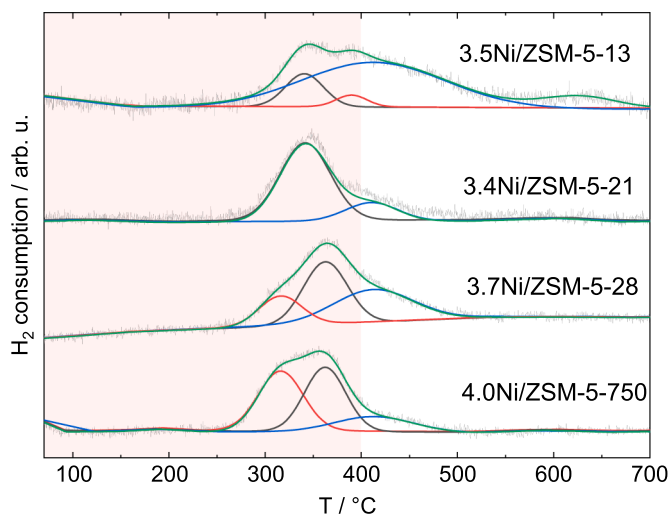


Fig. 2. H_2 -TPR profiles of Ni supported on ZSM-5 zeolites with different Si to Al molar ratios (3.5Ni/ZSM-5-13, 3.4Ni/ZSM-5-21, 3.7Ni/ZSM-5-28 and 4.0Ni/ZSM-5-750). The red shaded area highlights the reduction temperature range (RT – 400 °C) prior to the catalytic experiments.

in the as synthesized catalysts, Ni is present as crystalline NiO and Ni^{2+} attached to zeolite framework acting as charge compensating cations, which can be referred to as extra framework Ni^{2+} cations (EFNi) [37].

The introduced Ni species are first seated as EFNi and then NiO. Thus, the number of NiO is inversely proportional to Al content of ZSM-5 zeolites provided a similar Ni content. In particular, at a ca. 3.5 wt.% Ni, 3.5Ni/ZSM-5-13 exhibits a considerably lower amount of NiO (0.245

$\text{mmol}\cdot\text{g}^{-1}$), while it is higher for 3.4Ni/ZSM-5-21 and 3.7Ni/ZSM-5-28, i.e., 0.417 and 0.448 $\text{mmol}\cdot\text{g}^{-1}$, respectively (Table 2).

The reducibility of Ni-containing species was further investigated by temperature-programmed reduction with H_2 (H_2 -TPR) and shown in Fig. 2. The overall shape of the TPR curves suggest that the morphology of NiO species differs among samples owing to Ni content and Al composition. Under identical conditions the majority of Ni^{2+} was reduced below 500 °C except for 3.5Ni/ZSM-5-13, which exhibits a small H_2 uptake at temperature above 550 °C. This could be associated with the abundance of framework Al in 3.5Ni/ZSM-5-13, which gives rise to the number of EFNi characterized by a higher reduction temperature in comparison to NiO [46,47]. H_2 consumption and relative amount of Ni^{2+} reduced were calculated and displayed in Table 2. The obtained results suggest higher H_2 consumption, corresponding better Ni reducibility, for 4.0Ni/ZSM-5-750 and 3.7Ni/ZSM-5-28, which were completely reduced, whereas only a partial reduction was recorded for others under the same conditions.

The morphology of 3.7Ni/ZSM-5-28 and 4.0Ni/ZSM-5-750 was characterized by STEM. In good agreement with the XAS results, the introduced Ni^{2+} are present mainly as NiO nanoparticles for 3.7Ni/ZSM-5-28 and 4.0Ni/ZSM-5-750 as shown in Fig. 3. Moreover, while NiO nanoparticles are evenly distributed on the surface of 4.0Ni/ZSM-5-750, they are visible in large clusters in the case of 3.7Ni/ZSM-5-28.

3.2. Vapor-phase hydrogenation of levulinic acid: a micokinetic study

The hydrogenation microkinetics of LA were investigated over a series of Ni/ZSM-5 catalysts. Scheme 2 shows the possible reaction pathways, where the color of each compound is the same as in the plot lines in the concentration profile line over the length of the catalytic bed.

In addition to GVL, the observation of PA, PL and PP confirms further

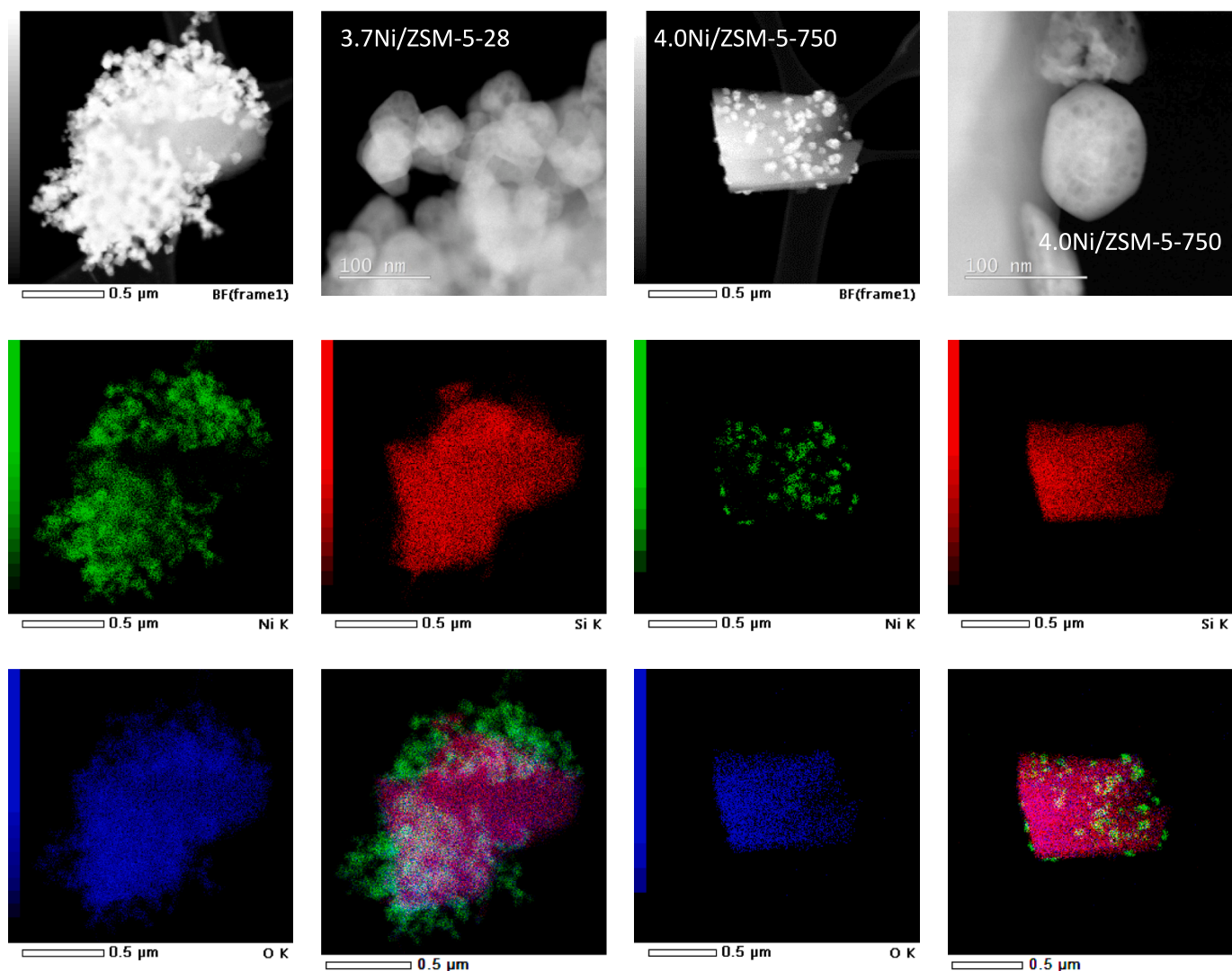
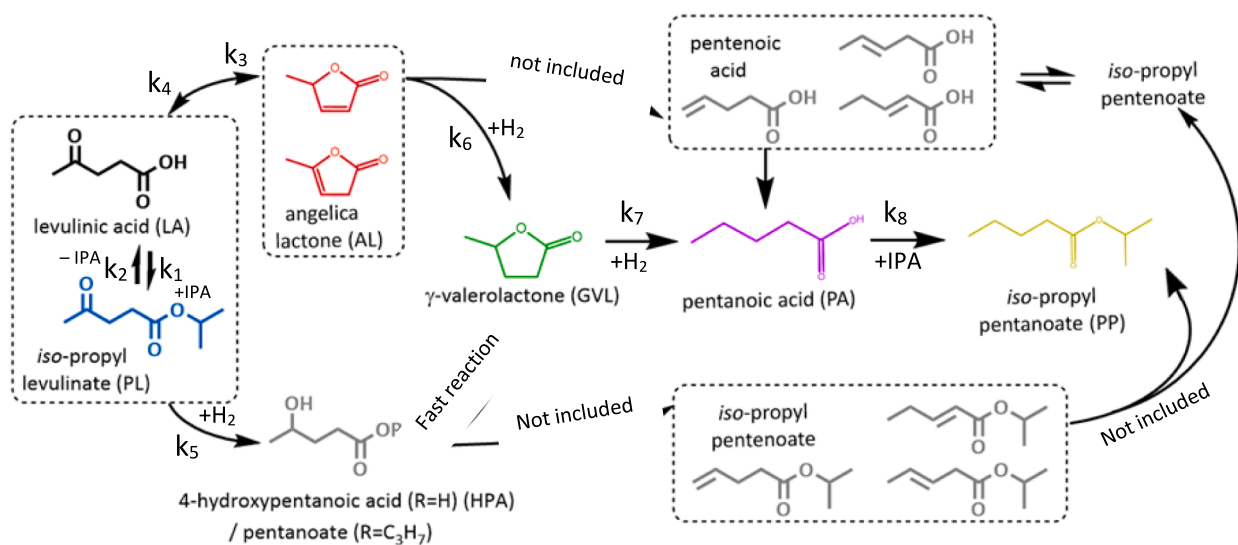


Fig. 3. HAADF-STEM micrographs and EDX elemental mapping including Ni (green), Si (red), O (blue) and overlaid image of 3.7Ni/ZSM-5-28 and 4.0Ni/ZSM-5-750.



Scheme 2. Proposed reaction pathway for LA hydrogenation in IPA displaying experimentally detected compounds in colors (LA: black, PL: blue, AL: red, GVL: green, PA: pink and PP: yellow) and undetected compounds in grey color.

hydrogenation and competitive acid-catalyzed esterification between solvent IPA and LA as well as IPA and PA as shown in Scheme 2. It is worth noting that the carbon mass balance of all experiments is above 93 %. The catalytic activity of all experiments is shown in Table S3.

To gain insight in the adsorption kinetics of both reactants (H_2 and LA), a pulse H_2 chemisorption, followed by H_2 -TPD and two temperature programmed desorption experiments were conducted and monitored by DRIFTS, in which LA was replaced with ethyl levulinate (EL) due to its lower boiling point. As GVL was not detected in the catalytic experiments conducted over bare H-ZSM-5 supports (Table S3), it is assumed that hydrogen adsorption and dissociation was possible only on nickel sites. Furthermore, the adsorption experiments of EL on 3.7Ni/ZSM-5-28 and ZSM-5-28 revealed that EL does not adsorb on nickel, or is not influenced by nickel, because the desorption rate is the same for both materials. Therefore, all compounds present in the reaction, apart from H_2 , adsorb on zeolite's acidic sites. If the reaction step requires hydrogen to proceed, the coverage fraction of the compound on the acid site is multiplied with the metallic active site coverage by hydrogen.

3.2.1. Pulse H_2 chemisorption and temperature-programmed desorption (TPD)

To determine the adsorption and desorption rate constants and the activation energy for the desorption reaction, a pulse H_2 chemisorption, followed by H_2 -TPD experiment was conducted on 4.0Ni/ZSM-5-750, which is described in the experimental section 2.2. The experimental and modelled data are shown in Fig. 4.

The modelled data are in good agreement with experimentally obtained H_2 fractions. With the regression analysis, the adsorption rate constant for H_2 k_{ads} was determined to be $3.8 \pm 0.7 \text{ min}^{-1}$, while the desorption rate constant k_{des} was $0.19 \pm 0.06 \text{ min}^{-1}$ at $250 \text{ }^\circ\text{C}$. The corresponding desorption activation energy was $26 \pm 5 \text{ kJ/mol}$. When the temperature increased, the desorption rate constant increased, which forced the desorption of H_2 . The calculated values were fed to the LA-reaction model, and held fixed during the regression analysis, to determine the reaction rate constant.

3.2.2. Ethyl levulinate and Iso-Propanol temperature programmed desorption

To determine the kinetic parameters of adsorption and desorption for LA, intermediates and products of the reaction pathway, temperature programmed DRIFTS experiments were conducted in the range of the temperatures, overlapping with catalytic reaction. As a descriptor for LA, ethyl levulinate (EL) was used. Fig. 5 shows that EL adsorbs more strongly on ZSM-5-28 than IPA. When the temperature reached $100 \text{ }^\circ\text{C}$, the fractional coverage of EL remains at 1, while more than 10 % of IPA

was desorbed. When the temperature reached $250 \text{ }^\circ\text{C}$, the fractional coverage of IPA is 20 %, while it is 60 % for EL.

The adsorption/desorption rate constants and the activation energy of desorption at $28 \text{ }^\circ\text{C}$ are shown in Table 3. As it was stated above, EL and similar species adsorb stronger than IPA, and thus the adsorption constant is higher. The desorption rate constant at the given temperature is lower than adsorption rate constant at ambient temperature for each compound. Activation energy for desorption is higher for EL than for IPA, which means that desorption rate constant would change its value to a greater extent despite the same temperature ramp rate.

3.2.3. LA hydrogenation in IPA

Irrespective of the catalysts, AL is detected in almost all of the product mixtures, suggesting that the formation of GVL most likely proceeds via dehydration, followed by hydrogenation as reported under similar conditions [39,48,49]. Although 4-hydroxy pentanoic acid (HPA) was absent in the reaction mixtures (Fig. S6), the reaction pathway via HPA cannot be excluded. In other words, the catalytic transfer hydrogenation with *iso*-propanol acting as hydrogen source appears to occur only to a limited extent. Our microkinetic study suggests that the dominant pathway towards GVL is the esterification reaction and consecutive hydrogenation to GVL as shown in Fig. 6. When AL was used as reactant in the short catalyst bed length (5.5 mm) with 3.7 Ni/ZSM-5-28 catalyst at $210 \text{ }^\circ\text{C}$, LA, PL and consequently GVL were detected, which is shown in Fig. 7. Hence the reverse reaction of AL to LA is faster than the reaction of AL towards GVL. When PL is used as reactant, no LA is detected, while GVL is formed. When the higher temperature ($250 \text{ }^\circ\text{C}$) and longer catalyst bed (22 mm) were tested, similar yields of GVL and PA were obtained, as with LA as reactant. The accumulation of PL at longer residence time should lower the yield of GVL if the dominant reaction pathway was through AL intermediate, but this was not observed. The same phenomenon was observed for 4.0Ni/ZSM-5-750 catalyst. The corresponding data is shown in Table S3.

3.2.4. The influence of Al and Ni content of the bifunctional Ni/ZSM-5 catalysts

Firstly, the hydrogenation of LA was carried out using Ni catalysts supported on ZSM-5-21 with Ni content varied from 0.8 to 4.4 wt.%. Fig. 7 shows the predicted concentration profiles over the length of the catalyst bed. The estimated reaction rate constants are presented in Table S4.

While the gradually increasing Ni content has marginal influence on the LA conversion, the formation of the targeted product GVL rises significantly from 2 % up to 43 % at Ni content of 0.8 wt.% and 3.4 wt.%, respectively (Fig. 8). The GVL yield, however, drops to 11 % when Ni content reaches 4.4. wt.%. This is likely due to lower Ni dispersion and lower reducibility of 4.4Ni/ZSM-5-21. Despite the higher Ni content, 4.4Ni/ZSM-5-21 exhibits a similar H_2 consumption ($\approx 0.36 \text{ mmol}\cdot\text{g}^{-1}$) as 3.4Ni/ZSM-5-21, which indicates that the active Ni^0 could be less accessible, probably due to lower Ni dispersion. The observed trend of GVL yield suggest that the hydrogenation activity forming GVL is strongly associated with the presence of NiO nanoparticles which can be used as an indirect measure of metallic Ni^0 , as NiO are reduced during catalyst activation protocol. Additionally, no GVL was detected over bare ZSM-5-21 under identical conditions confirming that bare H-ZSM-5 is not active for the hydrogenation of LA into GVL. These observations indicate a key role of Ni sites in the conversion of LA into GVL. The reaction rate constant for reaction no. 5 was the highest for 3.7Ni/ZSM-5-28 catalyst (Fig. 8, right), indicating a superior hydrogenation capability among the tested catalysts.

Furthermore, the influence of Al content in the reaction pathway of LA conversion was investigated. The series of Ni/ZSM-5 with different Si to Al molar ratios (n_{Si}/n_{Al}) were tested under identical conditions ($250 \text{ }^\circ\text{C}$, atmospheric pressure). Irrespective of the catalyst used, the product mixtures consist of the intermediate AL, GVL as well as of esterification product PL. Interestingly, PA, the further hydrogenated

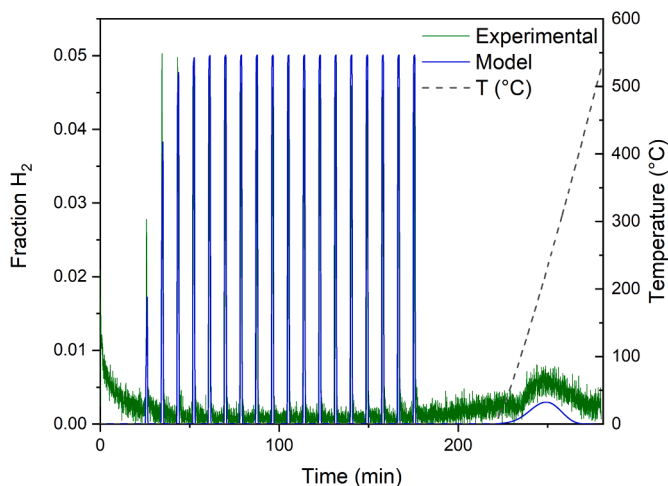


Fig. 4. Pulse H_2 adsorption and H_2 -TPD experimental (green line) and modelled data (blue line) of 4.0Ni/ZSM-5-750.

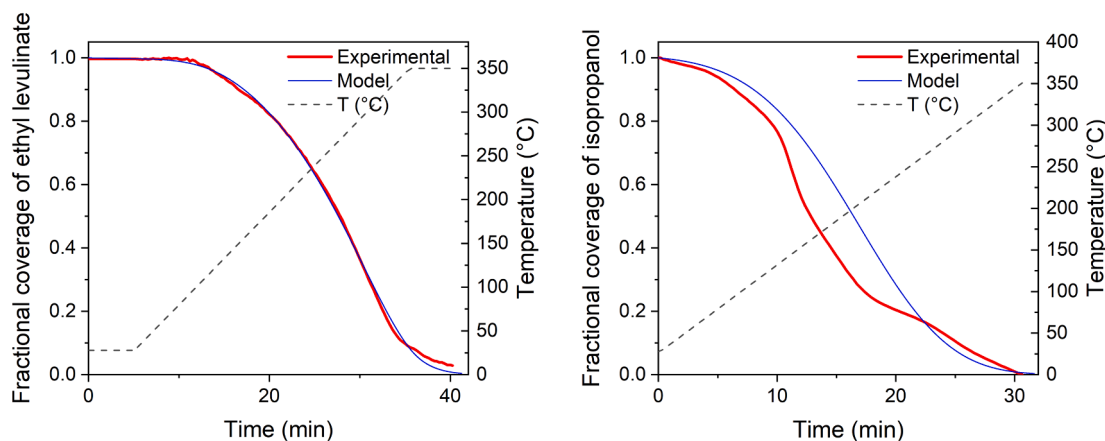


Fig. 5. Fractional coverage of active acid sites of EL (left) and IPA (right) on ZSM-5-28.

Table 3

Adsorption/desorption rate constants and activation energy of IPA and EL desorption determined by regression analysis.

	k_{ads} (min^{-1})	k_{des} (min^{-1})	E_{ades} (kJ/mol)
Iso-propanol	2.2 ± 0.2	0.0035 ± 0.0002	25 ± 2
Ethyl levulinate	133 ± 12	0.16 ± 0.01	38 ± 4

product of GVL, is only obtained over 3.7Ni/ZSM-5-28 and 4.0Ni/ZSM-5-750 suggesting that these two catalysts are the most active ones for the GVL synthesis in this study. With increasing Al content, i.e., lowering the Si to Al molar ratios from 28 to 13, both LA conversion and GVL yield decrease, whereas the yield of propyl levulinate (PL), the acid-catalyzed esterification product between LA and IPA solvent, arises from 13 % to 21 % and further to 47 %, respectively (Fig. 9, left). The boosting of PL

yield coupled with a decline of GVL yield suggests a clear competition between the two reactions. Furthermore, considering the similar Ni content (~ 3.5 wt.%), the higher ASD as a result of increasing Al content facilitates the esterification which outperformed the hydrogenation of LA into GVL. Consequently, a low Al content catalyst, e.g., 4.0Ni/ZSM-5-750, can accelerate the hydrogenation of PL to GVL and GVL to PA.

The correlation between GVL yield with NiO amount was examined (Fig. 9, right). A linear correlation is evidenced, proposing a close relation between the hydrogenation activity and Ni abundance. However, the linear fitting is no longer valid for 4.0Ni/ZSM-5-750 despite identical test conditions. 4.0Ni/ZSM-5-750 shows a much higher hydrogenation activity in comparison to 3.7Ni/ZSM-5-28. Particularly, a total yield of 16 % of PA and PP, further hydrogenated products, was recorded, which was only 1 % for 3.7Ni/ZSM-5-28 and not observed for other catalysts. Considering its similar structural and textural properties, 4.0Ni/ZSM-5-750 stands out as the outlier, likely attributed to the high

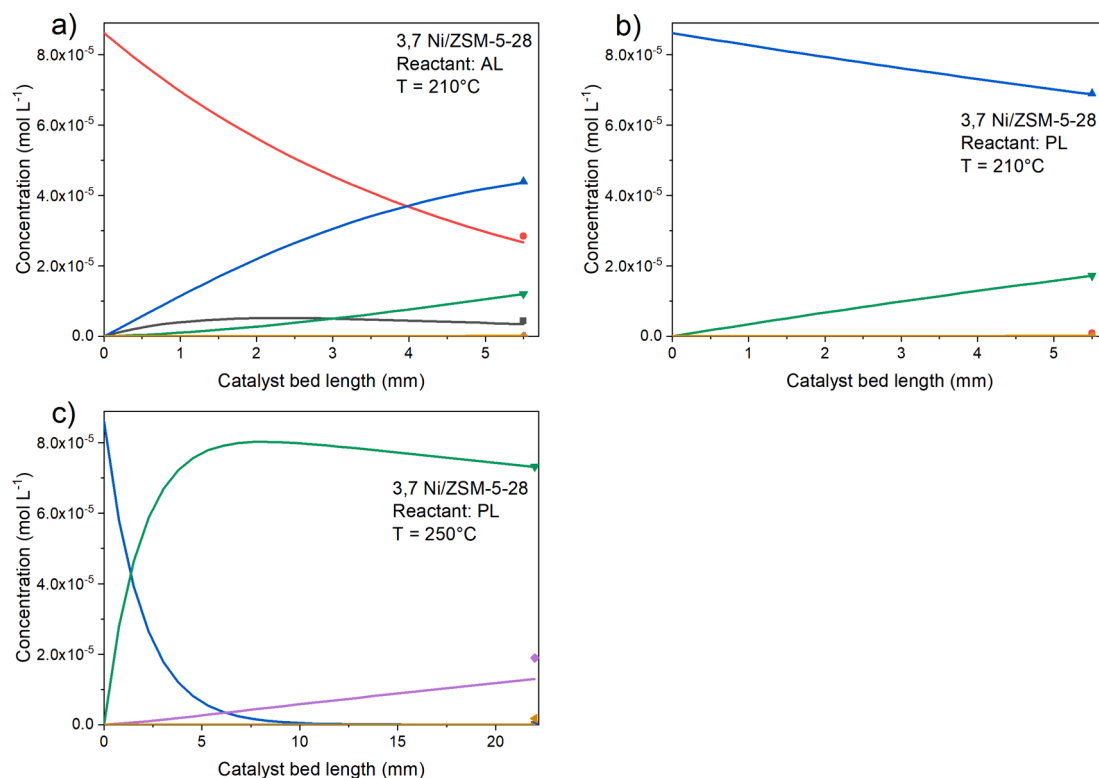


Fig. 6. Model predictions with AL and PL intermediates as reactants. a, b) short catalytic bed length of 5.5 mm and c) long catalytic bed length of 22 mm. The colors of each line match with the corresponding compounds in Scheme 2 above (LA: black, PL: blue, AL: red, GVL: green, PA: pink and PP: yellow).

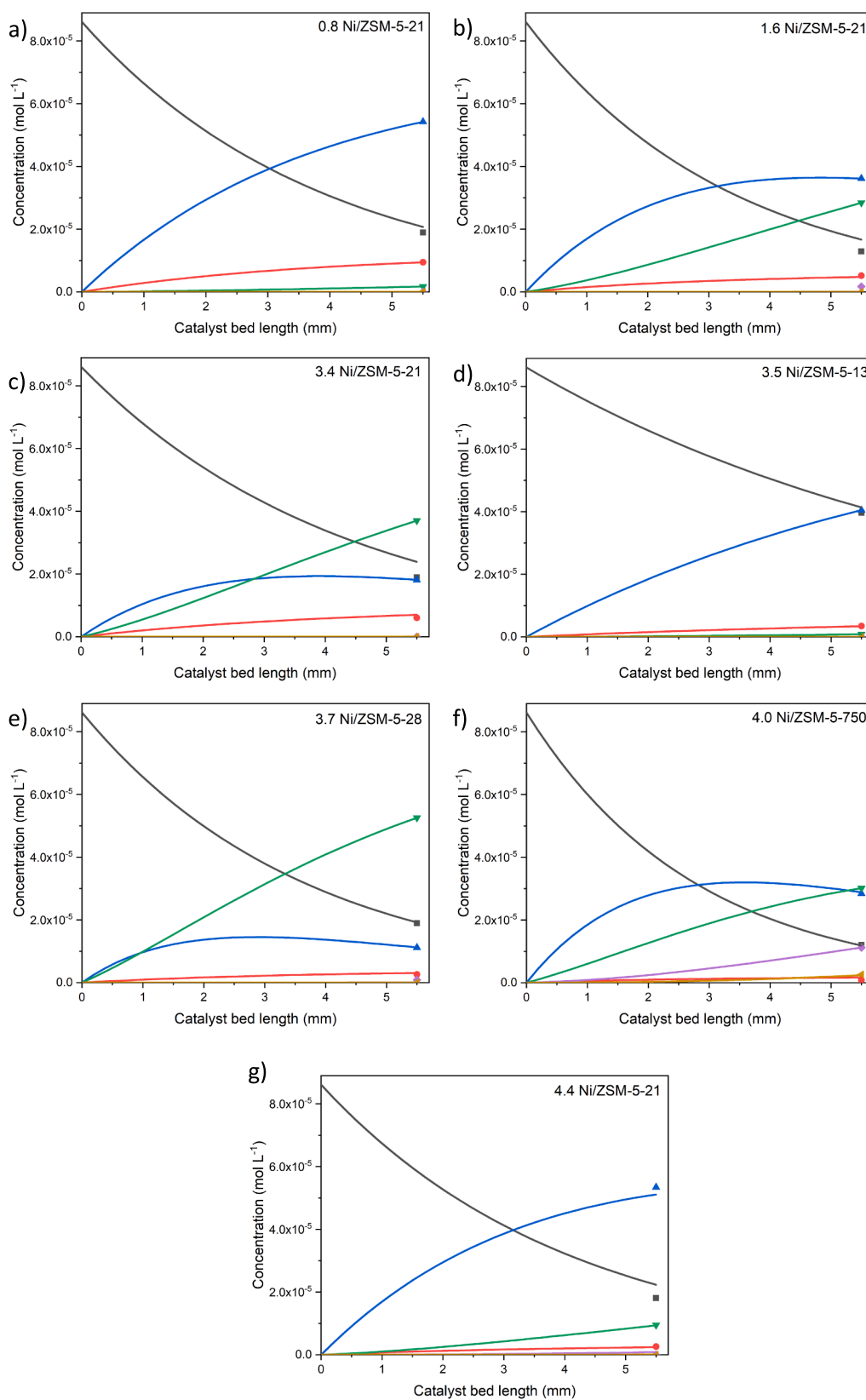


Fig. 7. Catalytic activity of Ni/ZSM-5 catalysts with various Ni content and Si/Al ratios in the hydrogenation of LA. Reaction conditions: $m_{\text{cat}} = 100 \text{ mg}$, $Q_{H_2} = 30 \text{ ml min}^{-1}$, $c_{LA} = 1 \text{ wt-\%}$, $Q_{LA} = 0.03 \text{ g min}^{-1}$, $250 \text{ }^\circ\text{C}$, 4 h. The colors of the symbols and the lines match the color in reaction pathway Scheme 2 (LA: black, PL: blue, AL: red, GVL: green, PA: pink and PP: yellow).

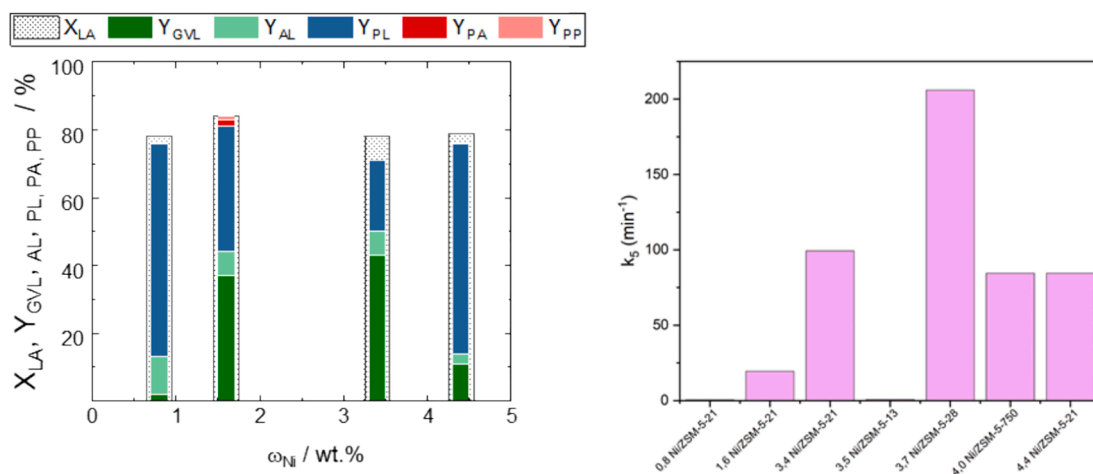


Fig. 8. LA conversion (X_{LA}) and products yield ($Y_{GVL, AL, PL, PA, PP}$) as a function of Ni content of the Ni/ZSM-5-21 (left) and reaction rate constant *no.* 5 values (k_5) in the hydrogenation of LA in IPA. Reaction conditions: $m_{cat} = 100$ mg, $Q_{H_2} = 30$ ml min⁻¹, $c_{LA} = 1$ wt-%, $Q_{LA} = 0.03$ g min⁻¹, 250 °C, 4 h.

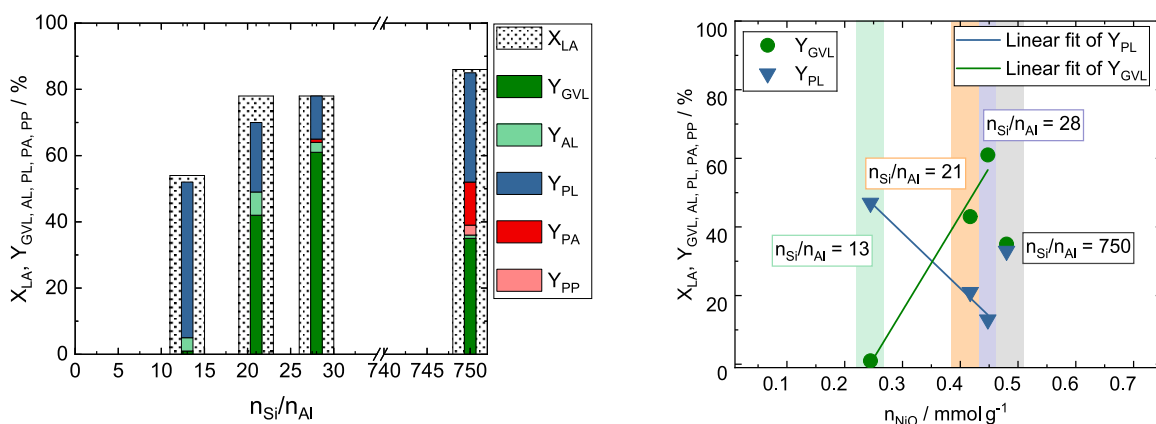


Fig. 9. LA conversion (X_{LA}) and products yield ($Y_{GVL, AL, PL, PA, PP}$) as a function of n_{Si}/n_{Al} (left) and as a function of NiO number (n_{NiO}) (right) of the catalysts, i.e., 3.5Ni/ZSM-5-13, 3.4Ni/ZSM-5-21 and 3.7Ni/ZSM-5-28. Reaction conditions: $m_{cat} = 100$ mg, $Q_{H_2} = 30$ ml·min⁻¹, $c_{LA} = 1$ wt%, $Q_{LA} = 0.03$ g·min⁻¹, 250 °C, 4 h. $n_{NiO} = (n_{Ni} \cdot \%NiO) / M_{Ni}$.

Ni dispersion and high Ni reducibility. These factors are crucial for the formation of PA, a further hydrogenated product from GVL, ultimately resulting in a low GVL yield.

3.2.5. Increased residence times and reaction's activation energy

To acquire the activation energy for all reaction steps, experiments with the two highly active catalysts 3.7Ni/ZSM-5-28 and 4.0 Ni/ZSM-5-750 were conducted employing two different catalyst bed length (5.5 and 22 mm) and at two reaction temperatures (210 and 250 °C). The obtained catalytic results are displayed in Fig. 10.

As mentioned above, the dominant pathway is the esterification reaction to PL (*No.* 1) followed by the hydrogenation to GVL (*No.* 5). This is further confirmed since a higher GVL yield was obtained upon increasing residence time via extending catalyst bed length. Regarding the activation energy, the results presented in Fig. 11 suggest a much higher esterification reaction's activation energy barrier for 4.0Ni/ZSM-5-750 compared to the highly acidic 3.7Ni/ZSM-5-28 catalyst. The dominance of strong acid sites, characterized by $T_{des} = 335$ –360 °C, in 4.0Ni/ZSM-5-750 (Table S1), likely facilitates the binding and retention of reactants, particularly with respect to LA. This phenomenon contributes to a substantial activation energy (E_a) for the esterification reaction. On the other hand, the 4.0Ni/ZSM-5-750 catalyst exhibits a lower activation energy barrier for reaction *No.* 5. This can be explained by the higher Ni dispersion (Fig. 3) and, consequently, a greater abundance of metallic Ni sites. These factors contribute to the enhancement

of the Ni-catalyzed hydrogenation reaction forming GVL as well as PA. The activation energy values for all the other reaction steps are shown in Table S5.

4. Conclusions

This study correlated the structure–activity relationship of Ni/ZSM-5 catalysts in vapor phase hydrogenation processes of LA. The interdependence of Ni and Al in bifunctional Ni/ZSM-5 catalysts played a crucial role in correlating hydrogenation forming GVL with the esterification of PL.

Furthermore, a novel microkinetic modeling approach, incorporating TPD, pulse chemisorption and DRIFT data to obtain kinetic parameters, was introduced. This method enables a deeper understanding of the ongoing reaction channels and paved the way for more accurate predictions of reaction pathways and the interplay of sorption and reaction phenomena on the catalyst surface. The study also revealed and quantified an alternative but dominant reaction pathway towards GVL, challenging the long-held perception of the process occurring through the formation of AL intermediates.

The 3.7Ni/ZSM-5-28 catalyst emerged as the optimal choice at 210 °C and under ambient pressure for obtaining GVL as the desired product. Notably, Al-rich catalysts with high acid site amounts and low metallic Ni active site concentrations favored esterification, reducing hydrogenation activity, and impeding further hydrogenation of GVL to

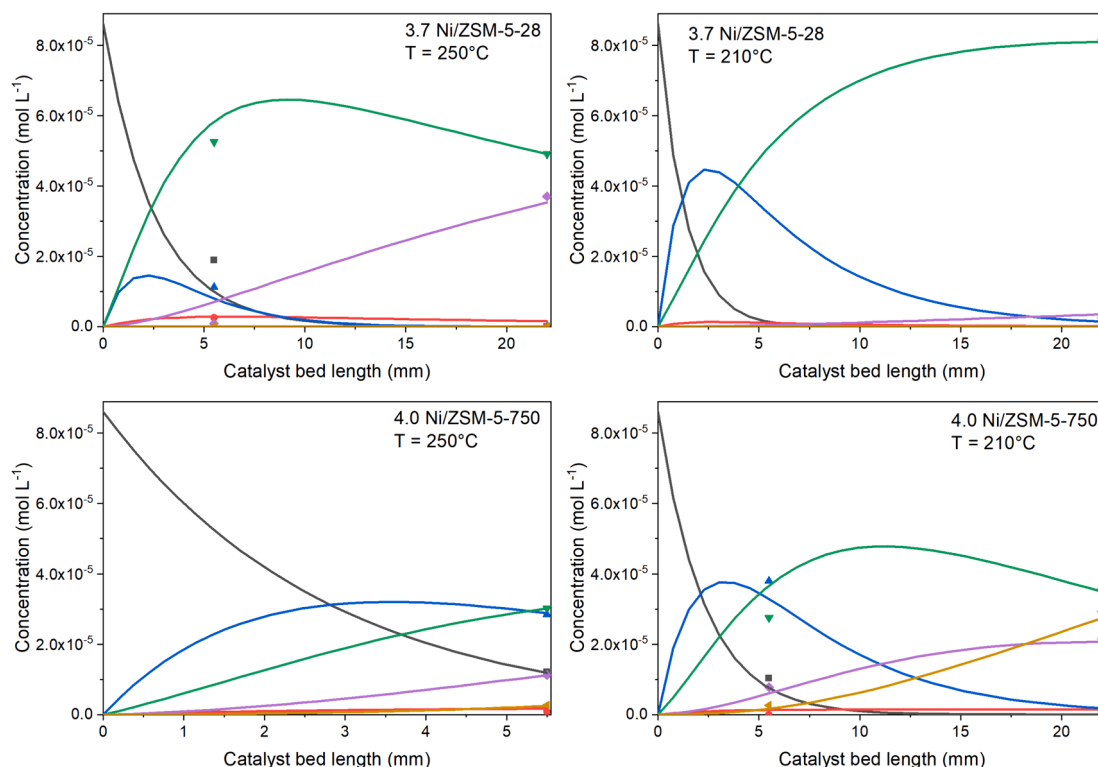


Fig. 10. Model predictions and experimental data at two different catalyst bed lengths and reaction temperatures. a,b) 3.7 Ni/ZSM-5-28, c,d) 4.0 Ni/ZSM-5-750. The colors of the symbols and the lines match the color in reaction pathway Scheme 2 (LA: black, PL: blue, AL: red, GVL: green, PA: pink and PP: yellow).

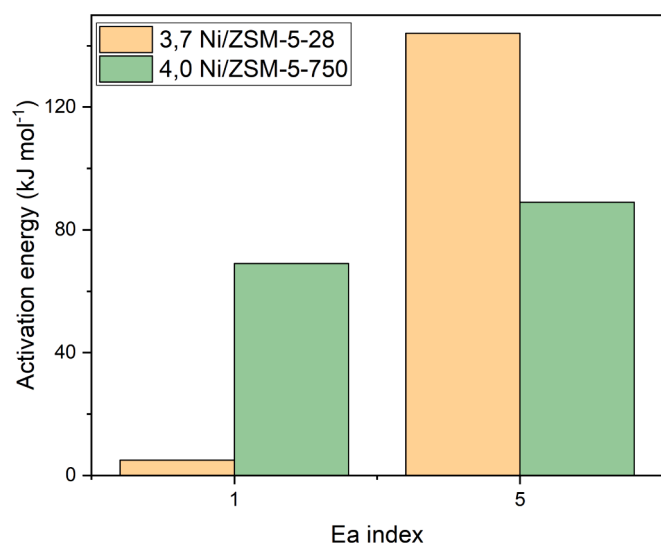


Fig. 11. Activation energy of two key reactions No. 1 and 5 in the hydrogenation of LA to GVL.

PA. To enhance PA formation, catalysts with a high Si to Al ratio, 4.0Ni/ZSM-5-750, was identified as crucial.

Finally, this comprehensive investigation not only emphasizes the versatility and bifunctional nature of Ni/ZSM-5 catalysts for vapor phase hydrogenation, but also introduces a pioneering microkinetic modeling approach. The obtained knowledge empowers the catalyst tailoring of product distribution, paving the way for more economical and environmentally friendly processes in the field or simply for deeper understanding of underlying phenomena.

CRediT authorship contribution statement

Hue-Tong Vu: Writing – original draft, Visualization, Methodology, Investigation, Formal analysis. **Žan Lavrič:** Writing – original draft, Methodology, Investigation, Formal analysis. **Andrii Kostyniuk:** Writing – original draft, Methodology, Formal analysis. **Goran Dražić:** Writing – original draft, Formal analysis. **Miha Grilc:** Writing – original draft, Supervision, Methodology, Investigation. **Blaž Likozar:** Writing – review & editing, Investigation, Funding acquisition. **Nataša Zabukovec Logar:** Writing – review & editing, Investigation, Funding acquisition. **Petar Djinović:** Writing – review & editing, Methodology, Investigation. **Nataša Novak Tušar:** Writing – review & editing, Supervision, Project administration, Investigation, Funding acquisition, Conceptualization.

Declaration of competing interest

The authors declare that they have no known competing financial interests or personal relationships that could have appeared to influence the work reported in this paper.

Data availability

Data will be made available on request.

Acknowledgements

Financial support from the Slovenian Research Agency (research programs P1-0021, P2-0152 and P1-0418) is acknowledged. The authors thank Manca Ocvirk and Suzana Mal for the synthesis of Ni/HZSM-5 catalysts, Edi Kranjc and Mojca Opresnik for XRD and SEM-EDX measurements, respectively. Additionally, the authors would like to express their deep gratitude to Urška Kavčič and Dimitrij Ješič for their unceasing support.

Appendix A. Supplementary data

Supplementary data to this article can be found online at <https://doi.org/10.1016/j.cej.2024.153456>.

References

- [1] A. Lambin, J.M. Corpart, UN sustainable development goals and green chemistry, key points for sustainably innovating at Roquette, a global leader in plant-based ingredients, *Curr. Opin. Green Sustain. Chem.* 13 (2018) 137–139, <https://doi.org/10.1016/j.cogsc.2018.04.007>.
- [2] E. Emmanouilidou, S. Mitkidou, A. Agapiou, N.C. Kokkinos, Solid waste biomass as a potential feedstock for producing sustainable aviation fuel: A systematic review, *Renew. Energy* 206 (2023) 897–907, <https://doi.org/10.1016/j.renene.2023.02.113>.
- [3] J.H. Clark, T.J. Farmer, L. Herrero-Davila, J. Sherwood, Circular economy design considerations for research and process development in the chemical sciences, *Green Chem.* 18 (2016) 3914–3934, <https://doi.org/10.1039/c6gc00501b>.
- [4] W. Deng, Y. Feng, J. Fu, H. Guo, Y. Guo, B. Han, Z. Jiang, L. Kong, C. Li, H. Liu, P.T. T. Nguyen, P. Ren, F. Wang, S. Wang, Y. Wang, Y. Wang, S.S. Wong, K. Yan, N. Yan, X. Yang, Y. Zhang, Z. Zhang, X. Zeng, H. Zhou, Catalytic conversion of lignocellulosic biomass into chemicals and fuels, *Green Energy Environ.* 8 (2023) 10–114, <https://doi.org/10.1016/j.gee.2022.07.003>.
- [5] V. Sharma, M.L. Tsai, P. Nargotra, C.W. Chen, P.P. Sun, R.R. Singhanika, A.K. Patel, C. Di Dong, Journey of lignin from a roadblock to bridge for lignocellulose biorefineries: A comprehensive review, *Sci. Total Environ.* 861 (2023) 160560, <https://doi.org/10.1016/j.scitotenv.2022.160560>.
- [6] J.N. Chheda, G.W. Huber, J.A. Dumesic, Liquid-phase catalytic processing of biomass-derived oxygenated hydrocarbons to fuels and chemicals, *Angew. Chem., Int. Ed.* 46 (2007) 7164–7183, <https://doi.org/10.1002/anie.200604274>.
- [7] M. Stöcker, Biofuels and biomass-to-liquid fuels in the biorefinery: Catalytic conversion of lignocellulosic biomass using porous materials, *Angew. Chem., Int. Ed.* 47 (2008) 9200–9211, <https://doi.org/10.1002/anie.200801476>.
- [8] J.J. Bozell, G.R. Petersen, Technology development for the production of biobased products from biorefinery carbohydrates—the US Department of Energy’s “Top 10” revisited, *Green Chem.* 12 (2010) 539–554, <https://doi.org/10.1039/B922014C>.
- [9] 360 Market Updates, Global levulinic acid market research report 2020, 2020. <https://www.360marketupdates.com/global-levulinic-acid-market-14828624>.
- [10] D. Di Menno Di, Y. Bucchianico, J.C. Wang, Y. Buvat, V.C. Pan, S.L. Moreno, Production of levulinic acid and alkyl levulinates: a process insight, *Green Chem.* 24 (2022) 614–646, <https://doi.org/10.1039/D1GC02457D>.
- [11] M. Sajid, U. Farooq, G. Bary, M.M. Azim, X. Zhao, Sustainable production of levulinic acid and its derivatives for fuel additives and chemicals: progress, challenges, and prospects, *Green Chem.* 23 (2021) 9198–9238, <https://doi.org/10.1039/D1GC02919C>.
- [12] W. Leitner, J. Klankermayer, S. Pischinger, H. Pitsch, K. Kohse-Höinghaus, Advanced biofuels and beyond: chemistry solutions for propulsion and production, *Angew. Chem., Int. Ed.* 56 (2017) 5412–5452, <https://doi.org/10.1002/anie.201607257>.
- [13] W.P. Xu, X.F. Chen, H.J. Guo, H.L. Li, H.R. Zhang, L. Xiong, X. De Chen, Conversion of levulinic acid to valuable chemicals: a review, *J. Chem. Technol. Biotechnol.* 96 (2021) 3009–3024, <https://doi.org/10.1002/jctb.6810>.
- [14] Z. Yu, X. Lu, J. Xiong, N. Ji, Transformation of levulinic acid to valeric biofuels: A review on heterogeneous bifunctional catalytic systems, *ChemSusChem* 12 (2019) 3915–3930, <https://doi.org/10.1002/cssc.201901522>.
- [15] R. Weng, Z. Yu, J. Xiong, X. Lu, Effects of water in the heterogeneous catalytic valorization of levulinic acid into γ -valerolactone and its derivatives, *Green Chem.* 22 (2020) 3013–3027, <https://doi.org/10.1039/D0GC01082K>.
- [16] S. Dutta, I.K.M. Yu, D.C.W. Tsang, Y.H. Ng, Y.S. Ok, J. Sherwood, J.H. Clark, Green synthesis of gamma-valerolactone (GVL) through hydrogenation of biomass-derived levulinic acid using non-noble metal catalysts: A critical review, *Chem. Eng. J.* 372 (2019) 992–1006, <https://doi.org/10.1016/j.cej.2019.04.199>.
- [17] O.A. Abdelrahman, A. Heyden, J.Q. Bond, Analysis of kinetics and reaction pathways in the aqueous-phase hydrogenation of levulinic acid to form γ -Valerolactone over Ru/C, *ACS Catal.* 4 (2014) 1171–1181, https://doi.org/10.1021/CS401177P/SUPPL_FILE/CS401177P_SI_001.PDF.
- [18] I.T. Horváth, H. Mehdi, V. Fábos, L. Boda, L.T. Mika, γ -Valerolactone—a sustainable liquid for energy and carbon-based chemicals, *Green Chem.* 10 (2008) 238–242, <https://doi.org/10.1039/B712863K>.
- [19] C. Moreno-Marrodan, P. Barbaro, Energy efficient continuous production of γ -valerolactone by bifunctional metal/acid catalysis in one pot, *Green Chem.* 16 (2014) 3434–3438, <https://doi.org/10.1039/C4GC00298A>.
- [20] A.S. Piskun, J.E. De Haan, E. Wilbers, H.H. Van De Bovenkamp, Z. Tang, H. J. Heeres, Hydrogenation of levulinic acid to γ -valerolactone in water using millimeter sized supported ru catalysts in a packed bed reactor, *ACS Sustain. Chem. Eng.* 4 (2016) 2939–2950, https://doi.org/10.1021/ACSSUSCHEMENG.5B00774/SUPPL_FILE/SC5B00774_SI_001.PDF.
- [21] C. López-Aguado, M. Paniagua, J.A. Melero, J. Iglesias, P. Juárez, M.L. Granados, G. Morales, Stable continuous production of γ -valerolactone from biomass-derived levulinic acid over Zr–Al-beta zeolite catalyst, *Catal.* 10 (2020) 678. <https://doi.org/10.3390/CATAL10060678>.
- [22] R. Gérardy, D.P. Debecker, J. Estager, P. Luis, J.C.M. Monbaliu, Continuous flow upgrading of selected C2–C6Platform chemicals derived from biomass, *Chem. Rev.* 120 (2020) 7219–7347, https://doi.org/10.1021/ACS.CHEMREV.9B00846/ASSET/IMAGES/MEDIUM/CR9B00846_0154.GIF.
- [23] A. Seretis, P. Diamantopoulou, I. Thanou, P. Tzevelekidis, C. Fakas, P. Lilas, G. Papadogiannakis, Recent advances in ruthenium-catalyzed hydrogenation reactions of renewable biomass-derived levulinic acid in aqueous media, *Front. Chem.* 8 (2020) 532503, <https://doi.org/10.3389/FCHEM.2020.00221/BIBTEX>.
- [24] J.M. Tukacs, M. Novák, G. Dibó, L.T. Mika, An improved catalytic system for the reduction of levulinic acid to γ -valerolactone, *Catal. Sci. Technol.* 4 (2014) 2908–2912, <https://doi.org/10.1039/C4CY00719K>.
- [25] A. Osatiashtiani, A.F. Lee, K. Wilson, Recent advances in the production of γ -valerolactone from biomass-derived feedstocks via heterogeneous catalytic transfer hydrogenation, *J. Chem. Technol. Biotechnol.* 92 (2017) 1125–1135, <https://doi.org/10.1002/jctb.5213>.
- [26] H. Zhang, M. Zhao, T. Zhao, L. Li, Z. Zhu, Hydrogenative cyclization of levulinic acid into γ -valerolactone by photocatalytic intermolecular hydrogen transfer, *Green Chem.* 18 (2016) 2296–2301, <https://doi.org/10.1039/C5GC02971F>.
- [27] L.T. Mika, I.T. Horváth, Homogeneous transition metal catalyzed conversion of levulinic acid to gamma-valerolactone, *Adv. Inorg. Chem.* 77 (2021) 1–25, <https://doi.org/10.1016/BS.ADIOCH.2021.02.004>.
- [28] Z. Yu, X. Lu, C. Liu, Y. Han, N. Ji, Synthesis of γ -valerolactone from different biomass-derived feedstocks: Recent advances on reaction mechanisms and catalytic systems, *Renew. Sustain. Energy Rev.* 112 (2019) 140–157, <https://doi.org/10.1016/j.rser.2019.05.039>.
- [29] M. Maumela, S. Marx, R. Meijboom, Heterogeneous Ru catalysts as the emerging potential superior catalysts in the selective hydrogenation of bio-derived levulinic acid to γ -valerolactone: effect of particle size, solvent, and support on activity, stability, and selectivity, *Catalysis.* 11 (2021) 292. <https://doi.org/10.3390/CATAL11020292>.
- [30] H.-T. Vu, F.M. Harth, M. Goepel, N. Linares, J. García-Martínez, R. Gläser, Enhanced activity of a bifunctional Pt/zeolite Y catalyst with an intracrystalline hierarchical pore system in the aqueous-phase hydrogenation of levulinic acid, *Chem. Eng. J.* 430 (2022), <https://doi.org/10.1016/j.cej.2021.132763>.
- [31] M. Al-Naji, J. Van Aelst, Y. Liao, M. D’Hullian, Z. Tian, C. Wang, R. Gläser, B. F. Sels, Pentanoic acid from γ -valerolactone and formic acid using bifunctional catalysis, *Green Chem.* 22 (2020) 1171–1181, <https://doi.org/10.1039/C9GC02627D>.
- [32] Z. Xue, Q. Liu, J. Wang, T. Mu, Valorization of levulinic acid over non-noble metal catalysts: challenges and opportunities, *Green Chem.* 20 (2018) 4391–4408, <https://doi.org/10.1039/C8GC02001A>.
- [33] N. Jyoti Mazumdar, P. Kumar, M. Arredondo-Arechavala, N. Artioli ac, H. Manyar, Structure sensitivity of Cu supported on manganese oxide catalysts in levulinic acid hydrogenation, *Catal. Sci. Technol.* (2023), <https://doi.org/10.1039/D3CY01064C>.
- [34] Q. Xu, X. Li, T. Pan, C. Yu, J. Deng, Q. Guo, Y. Fu, Supported copper catalysts for highly efficient hydrogenation of biomass-derived levulinic acid and γ -valerolactone, *Green Chem.* 18 (2016) 1287–1294, <https://doi.org/10.1039/C5GC01454A>.
- [35] M.N.E.H. Belguendouz, J. Gancedo, P. Rapado, D. Ursueguía, Y. Patiño, L. Faba, A. Bahmani, E. Díaz, S. Ordóñez, Selective synthesis of γ -valerolactone from levulinic and formic acid over ZnAl mixed oxide, *Chem. Eng. J.* 414 (2021) 128902, <https://doi.org/10.1016/j.cej.2021.128902>.
- [36] N. Karanwal, M.G. Sibi, M.K. Khan, A.A. Myint, B. Chan Ryu, J.W. Kang, J. Kim, Trimetallic Cu–Ni–Zn/H-ZSM-5 catalyst for the one-pot conversion of levulinic acid to high-yield 1,4-pentanediol under mild conditions in an aqueous medium, *ACS Catal.* 11 (2021) 2846–2864, <https://doi.org/10.1021/acscatal.0c04216>.
- [37] H.T. Vu, I. Arcon, D.O. De Souza, S. Pollastri, G. Dražič, J. Volavšek, G. Mali, N. Zabukovec Logar, N. Novak Tušar, Insight into the interdependence of Ni and Al in bifunctional Ni/ZSM-5 catalysts at the nanoscale, *Nanoscale Adv.* 4 (2022) 2321–2331, <https://doi.org/10.1039/D2NA00102K>.
- [38] V. Mohan, C. Raghavendra, C.V. Pramod, B.D. Raju, K.S. Rama Rao, Ni/H-ZSM-5 as a promising catalyst for vapour phase hydrogenation of levulinic acid at atmospheric pressure, *RSC Adv.* 4 (2014) 9660, <https://doi.org/10.1039/c3ra46485g>.
- [39] M. Popova, P. Djinović, A. Ristić, H. Lazarova, G. Dražič, A. Pintar, A.M. Balu, N. N. Tušar, Vapor-phase hydrogenation of levulinic acid to γ -valerolactone over bifunctional Ni/HZSM-5 catalyst, *Front. Chem.* 6 (2018) 370564, <https://doi.org/10.3389/FCHEM.2018.00285/BIBTEX>.
- [40] P. Sun, G. Gao, Z. Zhao, C. Xia, F. Li, Acidity-regulation for enhancing the stability of Ni/HZSM-5 catalyst for valeric biofuel production, *Appl. Catal. B Environ.* 189 (2016) 19–25, <https://doi.org/10.1016/j.apcatb.2016.02.026>.
- [41] V.K. Velisjio, N. Gutta, J. Tardio, S.K. Bhargava, K. Vankudoth, A. Chatla, S. Medak, V. Akula, Hydrodeoxygenation activity of W modified Ni/H-ZSM-5 catalyst for single step conversion of levulinic acid to pentanoic acid: An insight on the reaction mechanism and structure activity relationship, *Appl. Catal. A Gen.* 550 (2018) 142–150, <https://doi.org/10.1016/j.apcata.2017.11.008>.
- [42] T. Fakin, A. Ristić, V. Mavrodinova, N. Zabukovec Logar, Highly crystalline binder-free ZSM-5 granules preparation, *Microporous Mesoporous Mater.* 213 (2015) 108–117, <https://doi.org/10.1016/j.micromeso.2015.04.010>.
- [43] A. Kostyniuk, D. Bajec, B. Likozar, Catalytic hydrogenation, hydrocracking and isomerization reactions of biomass tar model compound mixture over Ni-modified zeolite catalysts in packed bed reactor, *Renew. Energy* 167 (2021) 409–424, <https://doi.org/10.1016/j.renene.2020.11.098>.
- [44] J.J. Rehr, R.C. Albers, S.I. Zabinsky, High-order multiple-scattering calculations of x-ray-absorption fine structure, *Phys. Rev. Lett.* 69 (1992) 3397, <https://doi.org/10.1103/PhysRevLett.69.3397>.

- [45] K.A. Cychosz, R. Guillet-Nicolas, J. García-Martínez, M. Thommes, Recent advances in the textural characterization of hierarchically structured nanoporous materials, *Chem. Soc. Rev.* 46 (2017) 389–414, <https://doi.org/10.1039/C6CS00391E>.
- [46] W. Li, H. Wang, X. Wu, L.E. Betancourt, C. Tu, M. Liao, X. Cui, F. Li, J. Zheng, R. Li, Ni/hierarchical ZSM-5 zeolites as promising systems for phenolic bio-oil upgrading: Guaiacol hydrodeoxygenation, *Fuel* 274 (2020) 117859, <https://doi.org/10.1016/j.fuel.2020.117859>.
- [47] Z.P. Hu, C.C. Weng, C. Chen, Z.Y. Yuan, Catalytic decomposition of ammonia to CO_x-free hydrogen over Ni/ZSM-5 catalysts: A comparative study of the preparation methods, *Appl. Catal. A Gen.* 562 (2018) 49–57, <https://doi.org/10.1016/j.apcata.2018.05.038>.
- [48] R. Kuna, P. Balla, N.P. Rajan, B. Ponnala, S. Hussain, V.R.C. Komandur, Highly dispersed and ultra-small Ni nanoparticles over hydroxyapatite for hydrogenation of levulinic acid, *React. Kinet. Mech. Catal.* 135 (2022) 183–199, <https://doi.org/10.1007/S11144-021-02113-6/METRICS>.
- [49] P.P. Upare, J.-M. Lee, Y.K. Hwang, D.W. Hwang, J.-H. Lee, S.B. Halligudi, J.-S. Hwang, J.-S. Chang, Direct hydrocyclization of biomass-derived levulinic acid to 2-methyltetrahydrofuran over nanocomposite copper/silica catalysts, *ChemSusChem* 4 (2011) 1749–1752, <https://doi.org/10.1002/cssc.201100380>.